Design and Analysis of Virtual Synchronous Machines in Inductive and Resistive Weak Grids

Javier Roldán-Pérez, *Member, IEEE*, Alberto Rodríguez-Cabero, and Milan Prodanovic, *Member, IEEE*

***Abstract*—The term Virtual Synchronous Machine (VSM) commonly refers to the emulation of synchronous machines operation by using power electronics converters. However, a wider application of this control technique is still pending on further refinement of its design aspects and digital implementation. In this paper, a systematic approach to design the VSM parameters is introduced. First, a simplified third-order small-signal model of a VSM based on the conventional model of synchronous generators is developed. Unlike the existing works published in literature, the proposed model takes into account the effects of inductive and resistive weak grids. The model is then used to design the controller parameters by appropriately placing the poles of the closed-loop system. VSM robustness is studied for weak grids dominated by either inductance or resistance, and the aspects of digital control implementation are addressed. All the control system features and improvements were tested on a 15 kW prototype of a battery-supported VSM connected to a weak grid.**

***Index Terms*—AC-DC power converters, control systems, virtual synchronous machine, weak grids.**

I. Introduction

MODERN electricity networks are facing a challenge of a large scale deployment and integration of distributed energy resources based on different generation technologies. This fact has motivated changes in electricity network regulations that have become more restrictive with respect to the operation of conventional generation [1] and power converters [2]. The challenge is even more pronounced and present in weak grids because the network voltage and frequency are not constant as it is typically assumed in power converter controllers based on a Phase Locked Loop (PLL) [3]. A common solution for Voltage Source Converters (VSCs) connection to microgrids and weak grids are droop controllers, which have been studied in depth in [4].

A different approach to VSCs integration to power systems is to emulate the dynamics of synchronous machines and the term VSM is typically used to described its principles [5]. Some authors included internal current and voltage controllers in VSMs since current limiting and other issues can be implicitly solved [6]. In all these solutions the effects of the internal controller parameters have an important impact on the performance of the VSM. Therefore, the process of the tuning of controller parameters may be challenging [7]. Direct emulation of synchronous machines is also possible, although additional features need to be added to the VSM. This includes current limiting [8], power quality [9], operation during voltage sags [10], and transition between control modes [11]. However, the aspects related to the digital control implementation such as discretization have received less attention in recent publications [12].

The design of the VSM control parameters is not a trivial task because of the non-linearity present in this type of control. This issue has been mostly addressed in the literature by using small-signal analysis techniques that have been proven to be adequate for studying the dynamics of VSMs [13]. Dong and Chen [14] presented a method to design the parameters of a VSM. Several factors such as additional damping were included in the model and an analytic solution for the parameters was obtained for second- and third-order models. Another comprehensive study to select the parameters of a VSM was presented by Wu *et al.* [15]. A frequency-domain approach was proposed to accurately set stability margins. Other design methods based on frequency-domain alternatives can also be found in the literature [16]. Shintai *et al.* [17] presented a model that was used to place the poles of the active power controller. Also, a method to decouple active and reactive power controls was explained. Other authors have also investigated the connection of VSMs to weak grids [18]. However, in these references the effects of the weak grid on the performance of the VSM have been studied by assuming only inductive weak grids. In contrast to the existing published works, a third-order model that takes into account the coupling effects of the weak grid (either resistive or inductive) is considered in this paper.

Shuai *et al.* [19] presented a stability analysis of a VSM by using the bifurcation theory and a small-signal analysis was carried out. The effect of the coupling impedance was studied in detail. Liu *et al.* [20] presented an enhanced VSM that reduced oscillations in VSM-based microgrids. The proposed method damped active and reactive power transients and improved the overall microgrid performance. The use of adaptive schemes for the selection of the VSM parameters is also reported in the literature [21]. D'Arco *et al.* [22], [23] presented a

Manuscript received September 19, 2018; revised March 7, 2019 and June 21, 2019; accepted July 15, 2019. Date of publication July 22, 2019; date of current version November 21, 2019. This work presented was supported by the Community of Madrid Government, Spain, through the research project PRICAM (S2013/ICE-2933). Paper no. TEC-00943-2018. *(Corresponding author: Javier Roldan-Perez.)*

The authors are with Electrical Systems Unit, IMDEA Energy Institute, Móstoles 28935, Madrid, Spain (e-mail: javier.roldan@imdea.org; alberto.rodriguez@imdea.org; milan.prodanovic@imdea.org).

Color versions of one or more of the figures in this paper are available online at http://ieeexplore.ieee.org.

Digital Object Identifier 10.1109/TEC.2019.2930643

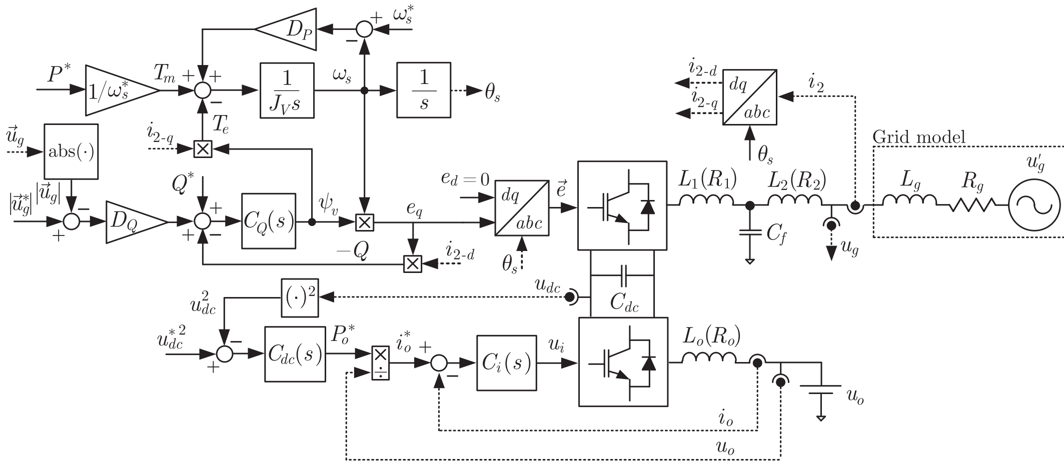

Fig. 1. Battery-supported VSM connected to a weak grid. The AC-DC VSC emulates a synchronous machine and provides voltage support and virtual inertia to the grid. The DC-DC VSC maintains the DC-link voltage constant.

parametric analysis of VSMs. The sensitivity of the closed-loop poles against variations in the system parameters was studied and the damping was optimised. State-space modelling was used, and the model provided an accurate description of the VSM dynamics. However, this type of model is too complex to be used at the design stage as the solutions for the VSM parameters cannot be obtained analytically. Dong and Chen [24] studied a method to reduce oscillations by adding a damping term to the VSM. Such approach yielded more degrees of freedom to the parameter selection, thus facilitating the design procedure.

In contrast to the previous studies, this paper features the conventional model commonly used to study synchronous machines for VSMs [25]. The contributions of this paper can be summarised as follows:

1) A simplified third-order small-signal model is developed. It will be demonstrated that the second order model commonly used to adjust the VSM parameters is a simplified version of this one. This model is based on the conventional synchronous generator model and takes into account the coupling between active- and reactive-power control loops. Compared to the works presented in the literature, the effects of the weak grid (both inductive and resistive) are taken into account during the design procedure.
2) An analytical solution for the steady-state values of the VSM is presented. This solution is an adaptation of the conventional method used for synchronous generators.
3) VSM robustness against grid impedance variations is explored for the case of resistive- and inductive-dominated weak grids. In particular, the impact of resistive weak grids is typically neglected in the literature.

All the proposed control improvements were tested on a 15 kVA prototype of a VSM with a 47.5 kWh Li-ion battery. The issues related to the discrete-time implementation, commonly ignored in the literature, are analysed here in detail.

II. Application and Controller Overview

A. Application Description

Fig. 1 shows the electrical and control diagram of a battery-supported VSM connected to a weak grid that was proposed in [12]. The grid-side converter provides voltage support and virtual inertia to the grid by emulating a synchronous generator. Meanwhile, the battery charger controls the DC-link voltage and manages the battery. The grid-side converter is connected to the PCC via a *LCL* filter, where L_1 and R_1 model the converter-side inductor, L_2 and R_2 model the grid-side inductor, and C_f is the filter capacitor. The effects of the weak grid are modelled by using L_g and R_g.

The grid-side current (i_2) and the grid voltage (u_g) are measured and used in the control system. A Synchronous Reference Frame (SRF) synchronized with the converter output voltage (e) is used for the controller implementation. The DC-link voltage (u_{dc}) is controlled by the DC-DC converter with a controller that sets the reference for the current controller $(i_o^* = P_o^*/u_o)$. The voltage generated by the battery converter is u_i and the voltage of the battery is u_o. The inductor of the DC-DC converter is modelled with L_o and R_o.

B. VSM Overview in a SRF

This section introduces the VSM control strategy that will be used in this paper. This formulation is an adaptation of the one previously proposed by Zhong and Weiss [26], and it can be also found in [12], [27].

The VSM virtual shaft can be modelled as:

$$J_V \cdot d\omega_s/dt = T_m - T_e + D_P(\omega_s^* - \omega_s) + T_d, \tag{1}$$

where ω_s is the synchronous frequency and ω_s^* is its set-point value, J_V is the virtual inertia, T_m is the motor torque, T_e is the electromagnetic torque, T_d is an additional damping term, and D_P is the droop coefficient. The main reason for including D_P is to provide the necessary power-frequency droop in steady state. However, this term also has an effect on the system damping [22], [23]. Depending on the application, this term may not provide sufficient damping and additional damping terms (included in T_d) should be added to the virtual shaft. This issue is studied in Section IV-C. The shaft rotation angle (θ_s) can be calculated as

$$d\theta_s/dt = \omega_s. \tag{2}$$

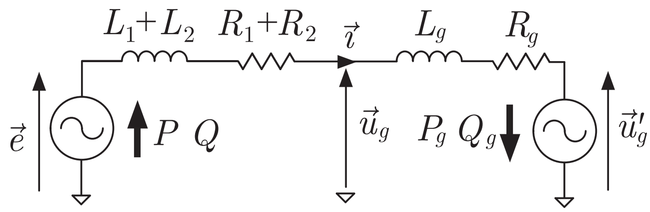

Fig. 2. Electrical diagram of a VSM connected to a weak grid. The filter capacitor of the *LCL* filter is neglected.

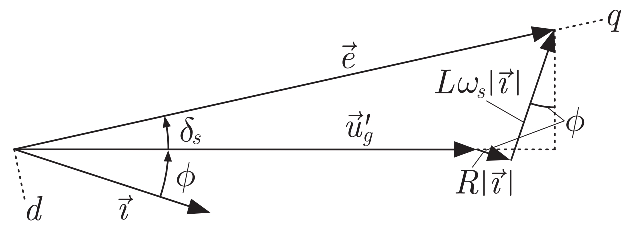

Fig. 3. Space-vector diagram of a VSM connected to the grid.

The SRF is synchronized with the q-axis of the VSM output voltage ($\vec{e}$) to simplify the formulation, thus:

$$e_q = \psi_v \omega_s \;\text{ and }\; e_d = 0, \tag{3}$$

where ψ_v will be called "virtual flux".

By using the instantaneous power theory, the active and reactive powers delivered by the VSC are:

$$P = \omega_s \psi_v i_q \;\text{ and }\; Q = \omega_s \psi_v i_d, \tag{4}$$

where i_d and i_q are calculated with the power-invariant Park's Transformation [28]. For the controller implementation, these variables will be calculated according to i_2 and u_g.

The electromagnetic torque for the shaft equation is:

$$T_e = P/\omega_s = \psi_v i_q, \tag{5}$$

while the motor torque can be expressed in terms of the active power set-point (P^*), yielding:

$$T_m = P^*/\omega_s \approx P^*/\omega_s^*, \tag{6}$$

since $\omega_s \approx \omega_s^*$ in steady state.

An integral controller acting on the virtual flux has been chosen to control the reactive power, thus

$$\psi_v = K_Q \int (Q^* + Q_D^* - Q)\, dt, \tag{7}$$

where Q^* is the reactive-power set point and K_Q is the integral controller gain. Grid-voltage support is provided by means of a droop controller that adds the term Q_D^* to the reactive-power set-point, thus

$$Q_D^* = D_Q(|\vec{u}_g^*| - |\vec{u}_g|), \tag{8}$$

where D_Q is the grid-voltage droop coefficient, $|\vec{u}_g|$ is the grid voltage space vector module, and $|\vec{u}_g^*|$ is its set point.

As shown before, the VSM active power injection is controlled by manipulating the VSM frequency, while the reactive power is controlled by modifying the virtual flux. This control strategy is effective in the case of inductively dominated grids. However, in the case of resistively-dominated weak grids, a coupling effect appears [29]. This effect is represented in the small signal model developed in this section and studied in detail in Section VI.

The effect of the filter capacitor below the fundamental frequency can be neglected because it is typically designed so that its effect has impact only in higher frequency range [30]. The electrical model depicted in Fig. 2 represents the AC-system dynamics if the filter capacitor is neglected, where P and Q are the active and reactive powers generated by the VSM, while P_g and Q_g are the active and reactive powers delivered to the grid. The filter equations are [31]:

$$L \cdot di_d/dt = -Ri_d - u'_{g-d} + \omega_s L i_q, \tag{9}$$

$$L \cdot di_q/dt = -Ri_q - u'_{g-q} - \omega_s L i_d + \omega_s \psi_v, \tag{10}$$

where $L = L_1 + L_2 + L_g$ and $R = R_1 + R_2 + R_g$.

III. VSM Small-Signal Model

A. Small-Signal Virtual Shaft Dynamics

The small-signal model of the virtual shaft described in (1) can be written as:

$$J_V \cdot d\Delta\omega_s/dt = \Delta T_m - \Delta T_e - D_P \Delta\omega_s + \Delta T_d, \tag{11}$$

where "Δ" stands for "incremental operator".

Assuming that $di_d/dt = di_q/dt = 0$ in (9) and (10):

$$i_d = \frac{\psi_v \omega_s^2 L - R|\vec{u}'_g| \sin\delta_s - \omega_s L |\vec{u}'_g| \cos\delta_s}{R^2 + \omega_s^2 L^2}, \tag{12}$$

$$i_q = \frac{\psi_v \omega_s R + \omega_s L |\vec{u}'_g| \sin\delta_s - R|\vec{u}'_g| \cos\delta_s}{R^2 + \omega_s^2 L^2}, \tag{13}$$

where $\vec{u}'_g = |\vec{u}'_g|(\sin\delta_s + j\cos\delta_s)$ and $\delta_s = \theta_s - \theta'_g$, as shown in Fig. 3 ($\theta'_g$ is the global angle of $\vec{u}'_g$). Under this premise the synchronous resonance of the connection filter is neglected [32]. Therefore, the order of the model is reduced and the system dynamics are easier to analyse. However, the proposed model is only accurate if the frequency of VSM poles is smaller than that of the synchronous resonance.

The electrical torque equation in (5) must be linearised to obtain ΔT_e. Therefore:

$$\Delta T_e = \Delta(\psi_v i_q) = K_{T\delta}\Delta\delta_s + K_{T\psi}\Delta\psi_v \tag{14}$$

with

$$K_{T\delta} = \left.\frac{\partial T_e}{\partial \delta_s}\right|_{x_o} = \frac{|\vec{u}'_g|\omega_s^o L \psi_v^o \cos\delta_s^o + |\vec{u}'_g| R \psi_v^o \sin\delta_s^o}{R^2 + (\omega_s^o)^2 L^2}, \tag{15}$$

$$K_{T\psi} = \left.\frac{\partial T_e}{\partial \psi_v}\right|_{x_o} = \frac{\omega_s^o L |\vec{u}'_g| \sin\delta_s^o - R|\vec{u}'_g| \cos\delta_s^o + 2\psi_v^o \omega_s^o R}{R^2 + (\omega_s^o)^2 L^2}, \tag{16}$$

where x_o is the operating point and the superscript "o" stands for steady-state value. The gain $K_{T\delta}$ represents the effect of active-power command (δ_s) on the active power injection (torque), while $K_{T\psi}$ represents the coupling effect between reactive-power command (ψ_v) and the active power injection.

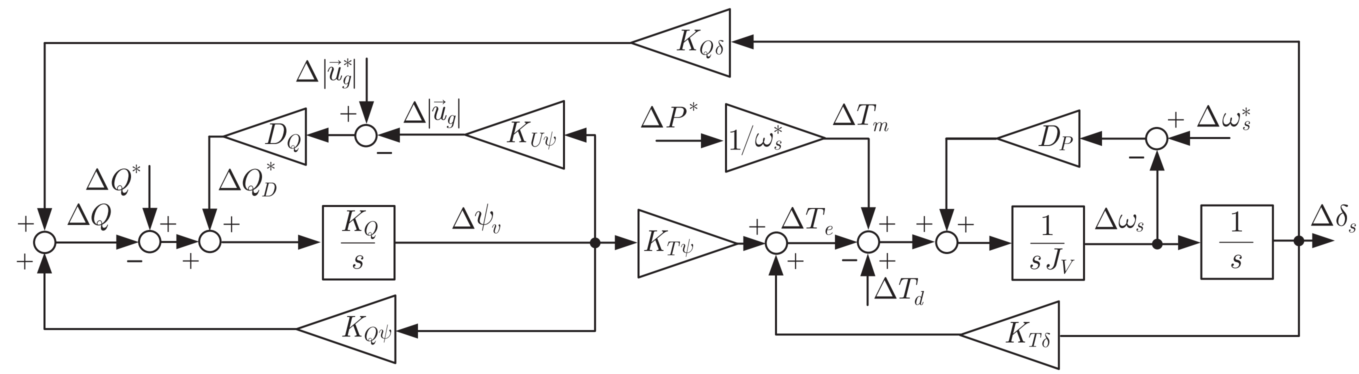

Fig. 4. Equivalent small-signal block diagram of a VSM in a weak grid. Gains $K_{T\delta}$, $K_{T\psi}$, $K_{Q\delta}$, $K_{Q\psi}$, and $K_{U\psi}$ are obtained by linearising the VSM model. Gains J_V, K_Q, D_P, and D_Q have to be designed according to the specific application.

B. Small-Signal Reactive Power Dynamics

The dynamics of Q are also non-linear (see (4)). The small-signal model can written as:

$$\Delta Q = \Delta(\omega_s \psi_v i_d) = K_{Q\delta}\Delta\delta_s + K_{Q\psi}\Delta\psi_v, \tag{17}$$

where

$$K_{Q\psi} = \left.\frac{\partial Q}{\partial \psi_v}\right|_{x_o} = \frac{2\psi_v^o L(\omega_s^o)^3 - |\vec{u}_g'|(\omega_s^o)^2 L\cos\delta_s^o - R|\vec{u}_g'|\omega_s^o \sin\delta_s^o}{R^2 + (\omega_s^o)^2 L^2}, \tag{18}$$

$$K_{Q\delta} = \left.\frac{\partial Q}{\partial \delta_s}\right|_{x_o} = \frac{\psi_v^o|\vec{u}_g'|(\omega_s^o)^2 L\sin\delta_s^o - R|\vec{u}_g'|\omega_s^o\psi_v^o\cos\delta_s^o}{R^2 + (\omega_s^o)^2 L^2}. \tag{19}$$

Gain $K_{Q\psi}$ represents the effect of reactive-power controller command (ψ_v) on the reactive power, while gain $K_{Q\delta}$ represents the coupling effect between the command for active power controller (δ_s) and the reactive power.

C. Small-Signal Grid Voltage Dynamics

If the grid is weak, the steady-state equation that links $\vec{e}$ with $\vec{u}_g$ can be written as

$$\vec{u}_g = \frac{L_g\omega_s j + R_g}{L\omega_s j + R}\vec{e} + \frac{(L_1+L_2)\omega_s j + (R_1+R_2)}{L\omega_s j + R}\vec{u}_g'. \tag{20}$$

Recalling that $e_d = 0$, the small-signal relation between $|\vec{u}_g|$ and $|\vec{e}| = e_q$ becomes:

$$\Delta|\vec{u}_g| = \sqrt{(L_g^2\omega_s^{o2} + R_g^2)/(L^2\omega_s^{o2} + R^2)}\cdot\Delta e_q. \tag{21}$$

In (21), input $\Delta u_g'$ is not included since it is not needed for the design the VSM parameters. To quantify the VSM effect over the grid voltage, the small-signal equation that links Δe_q with $\Delta\psi_v$ in (3) can be written as:

$$\Delta e_q = \Delta(\psi_c\omega_s) \approx \omega_s^o\Delta\psi_v + \psi_v^o\Delta\omega_s, \tag{22}$$

since ψ_v and ω_s operate close to their nominal values. For simplicity, it is assumed that $\omega_s^o\Delta\psi_v \gg \psi_v^o\Delta\omega_s$. This means that the effects of frequency variations over the grid voltage are neglected. By merging (21) and (22):

$$\Delta|\vec{u}_g| \approx K_{U\psi}\Delta\psi_v, \tag{23}$$

where

$$K_{U\psi} = \omega_s^o\sqrt{(L_g^2\omega_s^{o2} + R_g^2)/((L^2\omega_s^{o2} + R^2))}. \tag{24}$$

This expression includes the effects of inductive and resistive components of the weak grid.

D. Closed-Loop Transfer Functions

Fig. 4 shows the equivalent block diagram of the model developed in Section III-A, III-B, and III-C. The closed-loop transfer functions of this system can be obtained by applying block algebra to the system in Fig. 4 [33], yielding

$$F_T(s) = \frac{\Delta T_e(s)}{\Delta T_m(s)} = \frac{b_1^T s + b_0^T}{a_3 s^3 + a_2 s^2 + a_1 s + a_0}, \tag{25}$$

$$F_Q(s) = \frac{\Delta Q(s)}{\Delta Q^*(s)} = \frac{b_2^Q s^2 + b_1^Q s + b_0^Q}{a_3 s^3 + a_2 s^2 + a_1 s + a_0}, \tag{26}$$

where the coefficients are:

$$\begin{aligned}
a_0 &= K_Q K_{T\delta}(D_Q K_{U\psi} + K_{Q\psi}) - K_{Q\delta}K_{T\psi}K_Q,\\
a_1 &= D_P K_Q(D_Q K_{U\psi} + K_{Q\psi}) + K_{T\delta},\\
a_2 &= J_V K_Q(D_Q K_{U\psi} + K_{Q\psi}) + D_P,\\
a_3 &= J_V,\\
b_0^T &= K_Q K_{T\psi}K_{Q\delta} + K_{T\delta}K_Q(K_{Q\psi} + K_{U\psi}D_Q),\\
b_1^T &= K_{T\delta},\\
b_0^Q &= K_Q(D_P K_{Q\psi} + K_{T\delta}K_{Q\psi} - K_{T\delta}K_{T\psi}),\\
b_1^Q &= K_Q K_{Q\psi}D_P,\\
b_2^Q &= K_Q K_{Q\psi}J_V.
\end{aligned}$$

E. Operating Point

The operating point of the VSM can be obtained by using conventional methods commonly applied to synchronous machines [25], although some modifications are required. First of all, by assuming the ideal grid ($\vec{u}'_g$) has constant frequency (ω_g) and voltage levels:

$$\omega_s^o = \omega_g \text{ and } |\vec{u}_g'^o| = |\vec{u}'_g|. \tag{27}$$

To simplify the calculations, the active (P_g^o) and reactive (Q_g^o) powers delivered to $\vec{u}'_g$ are taken as inputs. Therefore, if the power-invariant Park's Transformation is used [34]:

$$|\vec{\imath}^o| = \sqrt{(P_g^o)^2 + (Q_g^o)^2}/|\vec{u}_g'^o|, \tag{28}$$

while the power-factor angle can be calculated as:

$$\phi^o = \cos^{-1}\left(P_g^o/\sqrt{(P_g^o)^2 + (Q_g^o)^2}\right). \tag{29}$$

From Fig. 3, the ideal grid voltage angle (δ_s^o) is [25]:

$$\delta_s^o = \tan^{-1}\left(\frac{L\omega_s^o|\vec{\imath}^o|\cos\phi^o - R|\vec{\imath}^o|\sin\phi^o}{|u_g'^o| + R|\vec{\imath}^o|\cos\phi^o + L\omega_s^o|\vec{\imath}^o|\sin\phi^o}\right). \tag{30}$$

The VSM output power (P) is required to calculate the virtual flux in (5). Therefore:

$$P^o = P_g^o + |\vec{\imath}^o|^2 R, \tag{31}$$

and the operating point for the virtual flux becomes:

$$\psi_v^o = P^o/(\omega_s^o i_q^o) = P^o/(\omega_s^o|\vec{\imath}^o|\cos(\delta_s^o + \phi^o)). \tag{32}$$

IV. Closed-Loop Pole Assignment Alternatives

A. Alternative 1: Third-Order Model Pole Assignment

With this alternative the poles of $F_T(s)$ are placed by selecting the VSM parameters. It is assumed that D_Q is fixed by the application, while D_P, J_V, and K_Q are the control parameters. Some remarks regarding the method proposed to select the VSM parameters:

1) Droop coefficient (D_P) is often set by the application requirements. In this case, an additional damping term is needed in the VSM controller [22], [24]. The selection of this damping term is addressed in Section IV-C.
2) The variable J_V is chosen to solve the third-order equation required to assign the closed-loop poles because it does not have the constraints of D_P.

Transfer function $F_T(s)$ can be parametrised with a pair of complex poles (ζ is the damping factor and ω_n is the natural frequency) and a single pole (ω_c is the cut-off frequency):

$$F_T(s) = \frac{N_T(s)}{s^3 + (\omega_c + 2\zeta\omega_n)s^2 + (\omega_n^2 + 2\zeta\omega_n\omega_c)s + \omega_c\omega_n^2}, \tag{33}$$

where $N_T(s)$ is the numerator polynomial. If coupling between active and reactive power is neglected, the complex poles (ω_n and ζ) are mainly related to the dynamics of the virtual shaft, while the single pole (ω_c) is mainly related with the dynamics of the reactive-power controller. These issues will be clarified in the following section where a simplified method to select the position of the closed-loop poles is studied.

The factors in the denominator of (25) can be identified with those of (33) and, after some algebraic calculations, the following equation can be obtained:

$$J_V^3 + c_2 J_V^2 + c_1 J_V + c_0 = 0, \tag{34}$$

where

$$c_0 = -K_{T\delta}/(AB)^2,\ c_1 = (\omega_n^2 + 2\zeta\omega_n\omega_c)/(AB)^2,$$
$$c_2 = -(2\zeta\omega_n + \omega_c)/(AB),$$
$$A = \omega_c\omega_n^2/(K_{T\delta} - K_{Q\delta}K_{T\psi}),\ B = D_Q K_{U\psi} + K_{Q\delta}.$$

The expression in (34) is a third-order equation that can be solved by using the Cardano's method [35], yielding:

$$J_V = S_A + S_B - c_2/3, \tag{35}$$

where

$$S_A = (R_A + (Q_A^3 + R_A^2)^{1/2})^{1/3},$$
$$S_B = (R_B - (Q_B^3 + R_B^2)^{1/2})^{1/3},$$
$$Q_A = (3c_1 - c_2)/9,\ R_A = (9c_1c_2 - 27c_0 - 2c_2)/54.$$

With J_V already found, D_P and K_Q can be calculated from the rest of the polynomial factors, yielding

$$D_P = (J_V(\omega_n^2 + 2\zeta\omega_n\omega_c) - K_{T\delta})/(J_V AB), \tag{36}$$

$$K_Q = \omega_c\omega_n^2/(K_{T\delta}B - K_{Q\delta}K_{T\psi}). \tag{37}$$

The third order equation (34) may have complex solutions for J_V and this should be avoided. The condition to guarantee that J_V is real can be written as follows [35]:

$$c_2^2 - 3c_1 > 0. \tag{38}$$

Equation (38) can be simplified, yielding:

$$(2\zeta\omega_n + \omega_c)^2 - 3(\omega_n^2 + 2\zeta\omega_n\omega_c) > 0. \tag{39}$$

Condition (39) only depends on the parameters of the closed-loop poles. Therefore, to guarantee that the solution for J_V is real it should be checked that the combination of ω_n, ζ, and ω_c used in the design meets (39). In addition to that, one should note that the proposed model has been developed by neglecting the synchronous resonance of the connection filter [16]. Therefore, the closed-loop poles should be significantly smaller than that particular resonant frequency.

B. Alternative 2: Simplified Pole Assignment

With this alternative, a simplified virtual-shaft model is used to select J_V and D_P, first. With these parameters already set, $F_T(s)$ is used to design K_Q. A simplified virtual-shaft transfer function ($\hat{F}_T(s)$) can be obtained assuming that $K_{T\psi} = K_{Q\delta} = 0$ in Fig. 4, thus

$$\hat{F}_T(s) = K_{T\delta}/(J_V s^2 + D_P s + K_{T\delta}). \tag{40}$$

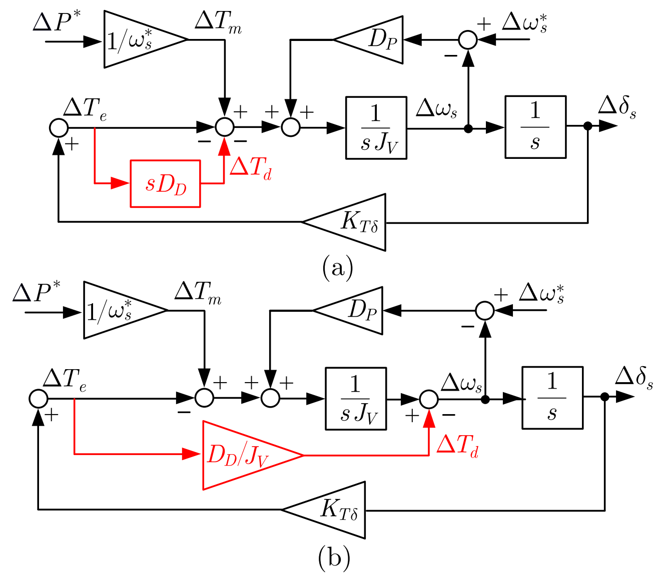

Fig. 5. Additional damping term that needs to be included if the droop coefficient is imposed by specific application requirements. (a) Conceptual idea and (b) practical implementation.

Defining the closed-loop poles with ζ and ω_n and identifying terms with a canonical second-order model [36]:

$$D_P = 2K_{T\delta}\zeta/\omega_n \text{ and } J_V = K_{T\delta}/\omega_n^2. \qquad (41)$$

It can be deduced from these results that the complex poles of the third-order model are mainly related to the active-power dynamics.

With D_P and J_V already set, the remaining pole of $F_T(s)$ (ω_c) can be placed with K_Q by using (37). Therefore, it can be seen that the simple pole of the third-order model is mainly linked to the reactive-power dynamics.

This simplified model is similar to the one that is commonly used in the literature [14], [15]. Therefore, this verifies that the proposed third-order model is a generalised case of that one.

C. Additional Damping Term

If the value of D_P is imposed by the application, a possible solution is to provide additional damping by adding the following damping torque to the virtual shaft, as suggested in [24]:

$$T_d = D_D \cdot dT_e/dt. \qquad (42)$$

The block diagram of the VSM including the additional term is depicted in Fig. 5(a). It can be seen that this term has an effect similar to that of a PD controller. However, in order to simplify its implementation and to avoid the derivative terms, the solution as in Fig. 5(b) is proposed.

By manipulating the block diagram, the following transfer function can be obtained:

$$\hat{F}_T = K_{T\delta}/(J_V s^2 + (D_P + D_D)s + K_{T\delta}). \qquad (43)$$

From (43), the value of D_D and J_V can be calculated.

$$D_D = 2K_{T\delta}\zeta/\omega_n - D_P \text{ and } J_V = K_{T\delta}/\omega_n^2. \qquad (44)$$

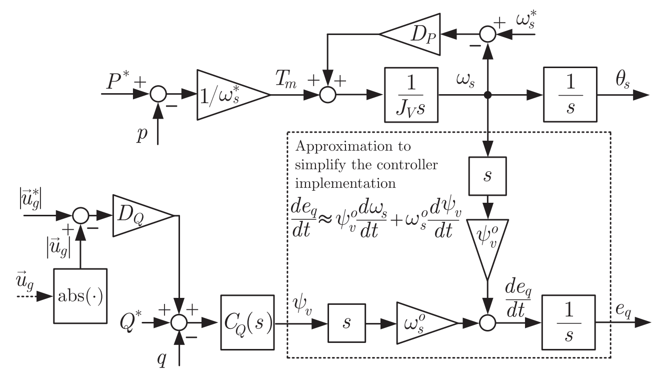

Fig. 6. Modified version of the VSM. The reactive-power controller integral is moved to the q-axis voltage command (e_q). A continuous-time (s) representation is used to simplify the explanation.

Now, the damping coefficient of the closed-loop poles can be tuned by using D_D even if the droop coefficient (D_P) is already set. This modification can be also included in the formulation of the third-order model. In that case, the coefficients presented in Section III-D should be recalculated taking into account this new term.

V. Controller Implementation

In this section, discrete-time implementation aspects of VSMs are described. This section represents an improved version of a part of conference paper [12].

A. Alternative Formulation for the Implementation

The electrical torque produced by the VSM can be written in terms of the electric power equation, giving:

$$T_e = p(t)/\omega_s \approx p(t)/\omega_s^*, \qquad (45)$$

$$p(t) = u_{g-d} \cdot i_{2-d} + u_{g-q} \cdot i_{2-q} \approx \omega_s \psi_v i_q, \qquad (46)$$

if the power-invariant Park's Transformation is used [34] and i_2 is taken as the control variable. The use of (46) to compute $p(t)$ instead of the internal variables makes the controller more practical since it will work in closed loop. Similarly, for the reactive power [28]:

$$q(t) = u_{g-q} \cdot i_{2-d} - u_{g-d} \cdot i_{2-q}. \approx \omega_s \psi_v i_d, \qquad (47)$$

if the power stored in the passive elements of the *LCL* filter is neglected [31]. Fig. 6 (left) shows the VSM controller when (46) and (47) substitute the original equations. It is worth pointing out that this controller resembles a Power Synchronisation Control (PSC) [32], except for the coupling term between ω_s and de_q/dt.

B. VSM Discretization

The VSM controller will be implemented in its incremental form [12], [37]. Therefore, all integrals are moved to the command signals (e_q and ω_s), as shown in Fig. 6 (right). This operation is typically done in discrete time, but here it is done in continuous time to facilitate the explanation, thus:

$$de_q/dt = d(\psi_v \omega_s)/dt = \omega_s \cdot d\psi_v/dt + \psi_v \cdot d\omega_s/dt. \qquad (48)$$

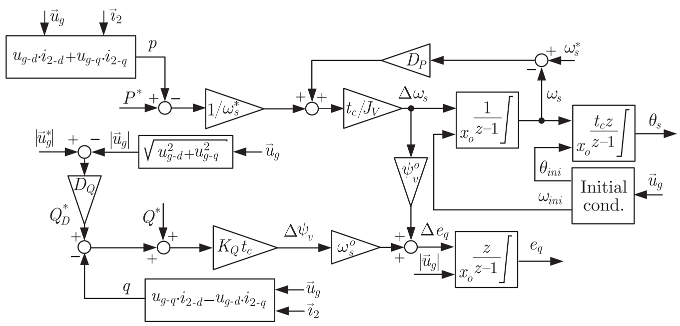

Fig. 7. Discrete-time incremental implementation of the proposed VSM control system. The meaning of physical variables has been maintained so that the controller is easy to understand.

TABLE I
PARAMETERS AND RATINGS OF THE SYSTEM ELEMENTS

Var.	Value	Var.	Value	Var.	Value
L_1	2.3 mH	S_n	15 kVA	L_o	5 mH
R_1	0.1 Ω	V_n	400 V	R_o	50 ,Ω
L_2	0.9 mH	f_n	50 Hz	C_f	8.8 μF
R_2	0.03 Ω	V_{dc}	680 V	C_{dc}	4 mF

Equation (48) is non-linear, however, the steady-state values of ω_s and ψ_v (ω_s^o and ψ_v^o) will be close to their nominal values regardless the operating point. Therefore:

$$de_q/dt \approx \omega_s^o \cdot d\psi_v/dt + \psi_v^o \cdot d\omega_s/dt. \tag{49}$$

This modification is depicted inside the dotted rectangle of Fig. 6. Fig. 7 shows the integrals of ω_s (θ_s) and de_q/dt (e_q) are discretised by using the backward Euler method:

$$\begin{aligned} \theta_s[k] &= \theta_s[k-1] + t_s \cdot \omega_s[k], \\ e_q[k] &= e_q[k-1] + t_s \cdot \Delta e_q[k], \end{aligned} \tag{50}$$

while the integral of $d\omega_s/dt$ (ω_s) is discretized by using the forward Euler method to avoid algebraic loops:

$$\omega_s[k] = \omega_s[k-1] + t_s \cdot \Delta\omega_s[k-1]. \tag{51}$$

Variable k stands for the sample number. The initial values of ω_s and θ_s are obtained from the grid-voltage space vector. The derivative terms in Fig. 6 are cancelled with integrals.

VI. Control System Analysis and Weak Grid Effect

The main system parameters are shown in Table I. The controller specifications were $\zeta = 1/\sqrt{2}$, $\omega_n = 5 \cdot 2\pi$, and $\omega_c = 10 \cdot 2\pi$ rad/sec. The value of D_Q was set to 50 to provide grid voltage support.

A. Stability Evaluation With the Closed-Loop Poles

Fig. 8 shows the poles of $F_T(s)$ for different scenarios. In Fig. 8(a) the active power delivered to the grid (P_g^o) varied from -1 to 1 pu (with $Q_g^o = 0$). In Fig. 8(b), Q_g^o varied between -1 and 1 pu (with $P_g^o = 0$). The VSM was robust against variations in P_g, and more sensitive to changes in Q_g^o. Fig. 8(c) shows the closed-loop poles obtained when L_g was modified (inductive weak grid). The complex poles moved in parallel to

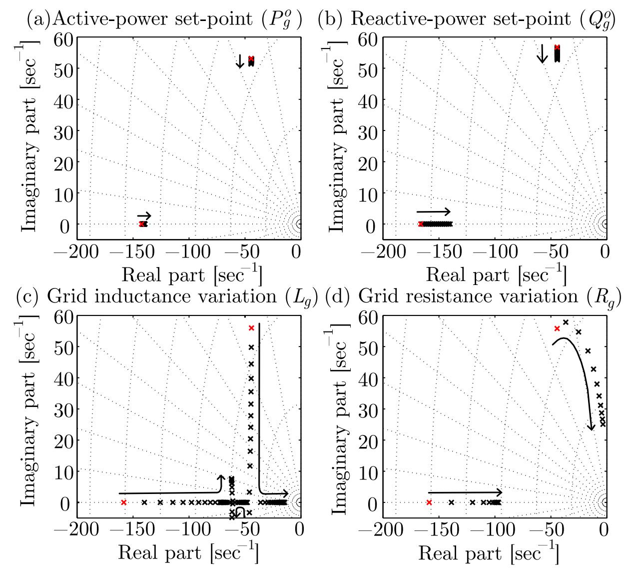

Fig. 8. Poles of $F_T(s)$ changing (a) P_g^o and (b) Q_g^o between -1 and 1 pu. Poles of $F_T(s)$ changing (c) L_g and (d) R_g between 0 and 0.4 pu. The arrow indicates the increase direction.

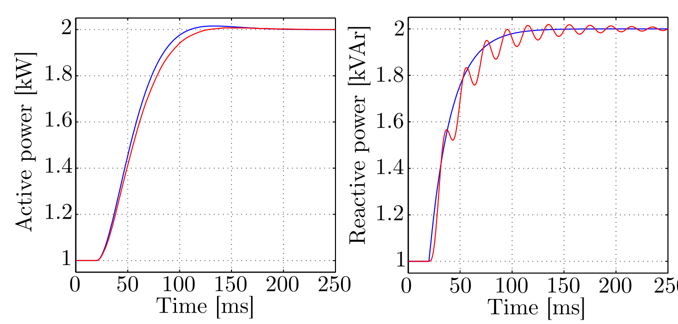

Fig. 9. Transient response of (red) the non-linear and (blue) the linear model, for step changes in (left) P^* and (right) Q^*. Simulation results, without grid impedance.

the imaginary axis until they reached the real axis. Since that moment, one pole approached the origin, while the other moved away until it reached the high-frequency real pole. Fig. 8(d) shows the closed-loop poles obtained when R_g was modified (resistive weak grid). The complex poles damping factor and natural frequency rapidly decreased when R_g increased, while the real pole approached the origin.

B. Model Validation

Fig. 9 shows the step responses of the VSM non-linear model and the proposed linearised model at the operating point of 400 V, 50 Hz, 1 kW, and 1 kVAr. The low-frequency dynamics of both models are similar, however, the simplified one does capture the synchronous oscillation that is more pronounced in the reactive-power transient. This oscillation is caused by the dynamics of the connection filter and adds a pair of resonant poles close to the fundamental frequency [32]. If the effect of the synchronous resonance is very pronounced, there are two possible ways to deal with the issue:

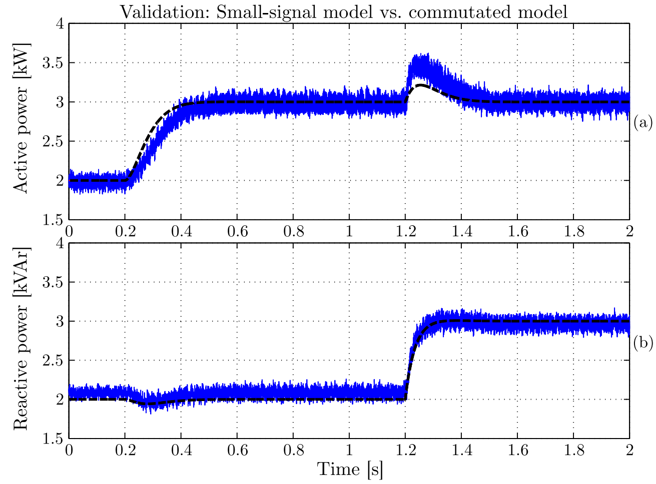

Fig. 10. Validation of the small-signal model (including inductive grid impedance). (a) Active and (b) reactive power injected by the VSM. (blue) Commutated model developed in SimPowerSystems and (black) linearised model.

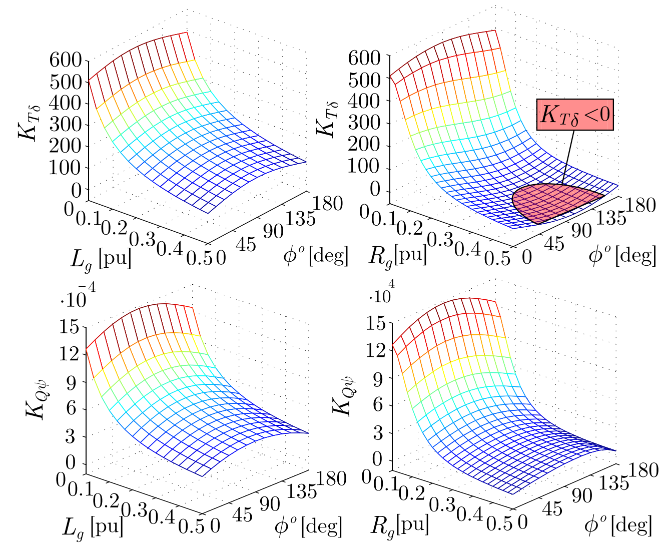

Fig. 11. Value of (top) $K_{T\delta}$ and (bottom) $K_{Q\psi}$, changing (left) L_g and (right) R_g. The power-factor angle is modified from 0 to 180 deg.

1) The first is to reduce the transient speed of the VSM in order to avoid interactions. From the practical point of view, this means that ω_n and ω_c should be considerably smaller than ω_s^*.
2) The second is to add a compensator to damp the resonance. A common solution is the application of the resistive virtual impedance [38], the use of a decoupling system [39], or the introduction of a current loop with a high-pass filter [32]

Reduction of the synchronous resonance effect in VSMs is highly recommended for practical applications in order to avoid its unwanted interactions with other elements connected to the grid.

Fig. 10 shows the results obtained by using the simulation model developed in Simulink and SimPowerSystems and the linearised model. Step changes were applied to the active and reactive power commands. The controller used for the simulation was the same one that was used to obtain the experimental results. The simulation included all the effects related to switching devices and discrete-time implementation, such as PWM, dead-time, and calculus delay. It can be seen the proposed model captured the essential dynamics of the VSM. However, there were minor differences in the coupling, especially in the reactive-power step change. This was expected because of the use of more realistic component models in the simulation.

C. Stability Limits for Weak Grids

The closed-loop system can become unstable under weak-grid conditions since the small-signal-model gains (e.g. $K_{T\delta}$) are calculated according to the operating point and the system parameters [25]. At least, two scenarios can take place when the active- or the reactive-power loops change their sign. In Fig. 4, it can be seen that this happens when $K_{Q\psi}$ and $K_{T\delta}$ become negative, respectively. Other sources of instability may also appear, but their effects are difficult to assess by analysing the sign of the gains of the small-signal model. Therefore:

1) The simplified virtual shaft in (6) will become unstable if $K_{T\delta} < 0$. From (15), $K_{T\delta} > 0$ is guaranteed if:

$$-\omega_s^o \cdot L/R < \tan\delta_s^o < \omega_s^o \cdot L/R, \quad (52)$$

where δ_s^o is calculated according to the operating point. The result in (52) is consistent with the poles depicted in Fig. 8(c) and (d). If L increases, the closed-loop poles move away from instability. However, when R increases, the damping factor decreases.
2) From Fig. 4, the sign of the reactive-power controller will change if $K_{Q\psi} < 0$, and this will happen once the numerator of (18) becomes zero. In this case:

$$L\omega_s^o > \cos(\delta_s^o + \phi^o)(L\omega_s^o \cos\delta_s^o + R\sin\delta_s^o)/2, \quad (53)$$

where ψ_v^o has been substituted by its operating point calculated with (32). Also, it has been assumed that $P_g^o \approx P^o$ to simplify the expression. Note that (53) will be always fulfilled if $L\omega_s^o > R/2$, and this is consistent with the results already obtained in this section.

Fig. 11(a) to (d) show the value of $K_{T\delta}$ and $K_{Q\psi}$ when the VSM generates its nominal apparent power, for different values of ϕ^o, R_g, and L_g. For inductive grids, $K_{T\delta} > 0$ and $K_{Q\psi} > 0$, always. However, for resistive grids $K_{T\delta}$ becomes negative, eventually, while $K_{Q\psi}$ approaches zero. This is realistic since the active power-angle and reactive power-voltage equations that are used in the VSM are only valid for inductive grids.

VII. Experimental Results

A. Experimental Platform

The proposed control system was tested at IMDEA Energy facilities [40]. The main parameters of hardware setup are shown in Table I. Resonances were neglected since parasitic resistances provided sufficient damping. The grid was emulated by another VSC connected via a LC filter ($L_1' = L_1$ and $C_f' = C_f$) that was operated in open-loop. Weak-grid scenarios were emulated

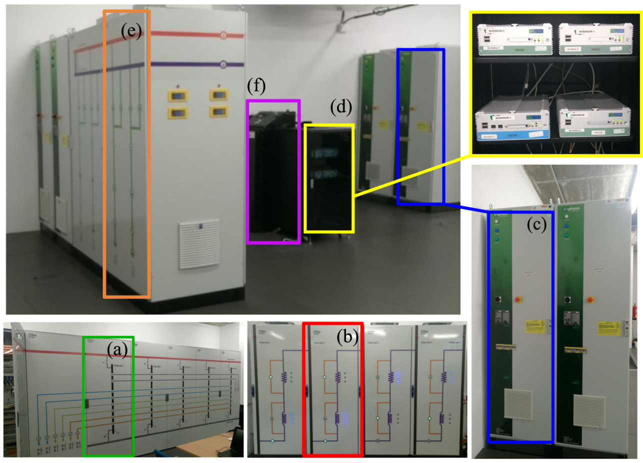

Fig. 12. Laboratory facilities. (a) AC busbars, (b) configurable impedances, (c) VSC, (d) embedded computers, (f) battery system, and (e) DC busbars.

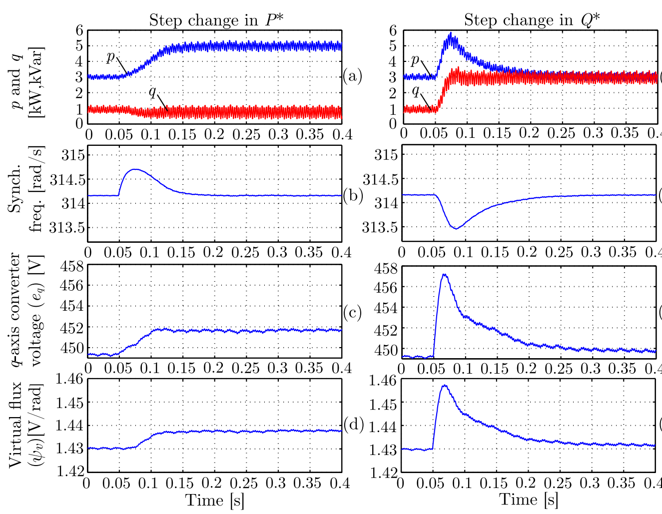

Fig. 13. Experimental results (from the prototype). VSM transient performance for step changes in (left) P^* and (right) Q^*.

by inserting resistances and (or) inductances between the VSM and the grid-emulating VSC. The battery charger was a two-leg two-level 90 kW interleaved VSC. The storage device was a 47.5 kWh Li-ion battery. The main components of the laboratory are depicted in Fig. 12.

The control system of the grid-side converter was implemented on an embedded PC [40]. The sampling and switching frequencies were 10 kHz. Pulse Width Modulation (PWM) with third harmonic injection and single update was used [31].

1) Transient Response (P^* and Q^* steps): Fig. 13 shows the active and reactive powers injected to the grid when a 2 kW (kVAr) step change was applied to P^* (Q^*). For the steps of P^* the grid current moved from its initial value to the set point, rapidly. For the step change of Q^*, the transient was faster and more coupled. The linear model described the system dynamics accurately. Also, the response of the implemented model resembles the response of the original VSM model. In both cases the frequency oscillated and, since the grid frequency was fixed, it returned to the initial value when the transient completed. In

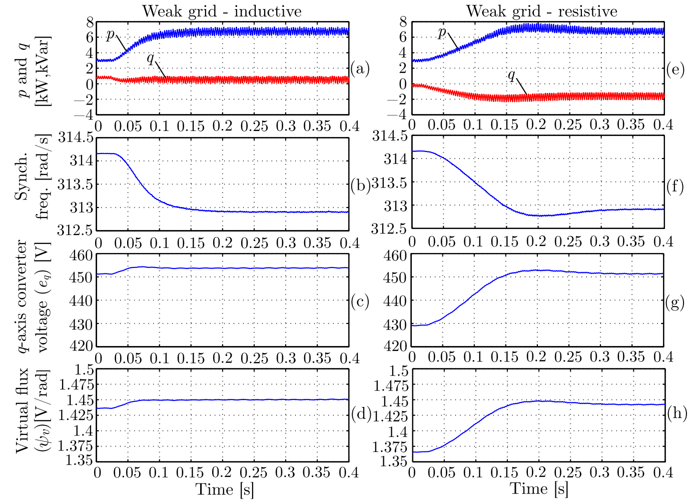

Fig. 14. Experimental results (from the prototype). Step-change of the grid frequency, weak-grid. (left) Inductive ($L_g = 0.2$ pu, $R_g = 0.04$ pu) and (right) resistive ($L_g = 0.07$ pu, $R_g = 0.3$ pu) weak grid.

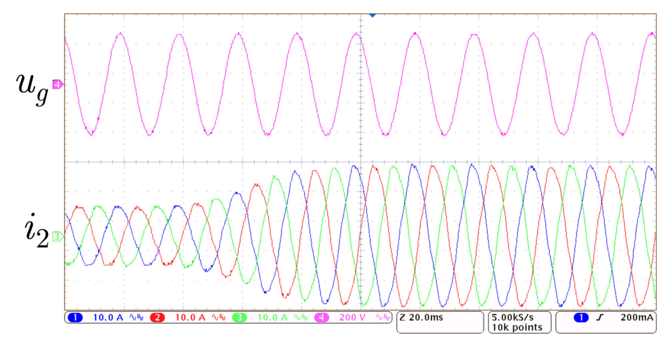

Fig. 15. Experimental results. Output current generated by the VSM when a step change was applied to P^*.

the reactive power transient there was a coupling between active and reactive power. This was expected because e_q is affected by both the frequency and voltage commands (see Fig. 1). To avoid this effect the coupling term in the VSM voltage command can be eliminated, yet this was not the case under studied in this paper.

2) Operation in a Weak-Grid Scenario: Fig. 14 (left) shows results obtained when the VSM was connected to an inductive weak grid ($L_g = 0.2$ pu and $R_g = 0.04$ pu). The maximum value of inductance available in the laboratory was used. The grid frequency suddenly changed from 50 Hz to 49.8 Hz. Therefore, the converter delivered 5.5 kW due to the active-power droop coefficient. Fig. 14 (right) shows the same test, but in this case the grid had a resistive characteristic ($R_g = 0.3$ pu and $L_g = 0.07$ pu). The maximum value of resistance available in the laboratory was used. The VSM remained connected to the grid, but the transient was slow and less damped. The coupling between the active and reactive powers increased due to the resistive weak-grid effect.

3) Output Current Waveform: Fig. 15 shows the output current for a step change of 4 kW in P^*. The current contains low-frequency harmonics (THD is 4.6%). To solve this issue, a dedicated controller can be added [27], but it was not included in this case in order to validate the proposed model without modifying the VSM dynamics.

VIII. Conclusion

This paper has addressed the application of grid-connected VSMs that provide voltage support and virtual inertia functionalities to a weak grid. A simplified small-signal model was developed and a method for the VSM parameters design proposed. This model successfully captures the low-frequency dynamics of the VSM apart from the synchronous resonance effect.

It has been shown that VSMs are robust against varying operating point. In addition to that, VSM robustness against variations of the grid impedance (L_g and R_g) was explored analytically and validated experimentally. This has been studied in two different ways: firstly the trajectory of the closed-loop was evaluated and secondly the signs of the relevant gains in the small-signal model were analysed against any changes of grid impedance. In both cases, it was shown that, unlike inductively-dominated grids, resistively-dominated weak grids may destabilise VSMs. All the control algorithms were tested on a 15 kW prototype where the controller was discretized and implemented in its incremental form.

Acknowledgment

The authors would like to thank Adrián González-Cajigas for the help with the additional damping term.

References

[1] L. Díez-Maroto, L. Rouco, and F. Fernández-Bernal, "Fault ride through capability of round rotor synchronous generators: Review, analysis and discussion of European grid code requirements," *Electric Power Syst. Res.*, vol. 140, pp. 27–36, 2016.

[2] J. Roldán-Pérez, A. García-Cerrada, J. L. Zamora-Macho, and M. Ochoa-Giménez, "Helping all generations of photo-voltaic inverters ride-through voltage sags," *IET Power Electron.*, vol. 7, no. 10, pp. 2555–2563, 2014.

[3] N. Pogaku, M. Prodanovic, and T. C. Green, "Modeling, analysis and testing of autonomous operation of an inverter-based microgrid," *IEEE Trans. Power Electron.*, vol. 22, no. 2, pp. 613–625, Mar. 2007.

[4] D. E. Olivares *et al.*, "Trends in microgrid control," *IEEE Trans. Smart Grid*, vol. 5, no. 4, pp. 1905–1919, Jul. 2014.

[5] S. D'Arco and J. A. Suul, "Equivalence of virtual synchronous machines and frequency-droops for converter-based microgrids," *IEEE Trans. Smart Grid*, vol. 5, no. 1, pp. 394–395, Jan. 2014.

[6] O. Mo, S. D'Arco, and J. A. Suul, "Evaluation of virtual synchronous machines with dynamic or quasi-stationary machine models," *IEEE Trans. Ind. Electron.*, vol. 64, no. 7, pp. 5952–5962, Jul. 2017.

[7] S. D'Arco, J. A. Suul, and O. B. Fosso, "Automatic tuning of cascaded controllers for power converters using eigenvalue parametric sensitivities," *IEEE Trans. Ind. Appl.*, vol. 51, no. 2, pp. 1743–1753, Mar. 2015.

[8] Z. Shuai, W. Huang, C. Shen, J. Ge, and Z. J. Shen, "Characteristics and restraining method of fast transient inrush fault currents in synchronverters," *IEEE Trans. Ind. Electron.*, vol. 64, no. 9, pp. 7487–7497, Sep. 2017.

[9] G. Li *et al.*, "Virtual impedance-based virtual synchronous generator control for grid-connected inverter under the weak grid situations," *IET Power Electron.*, vol. 11, no. 13, pp. 2125–2132, 2018.

[10] V. Natarajan and G. Weiss, "Synchronverters with better stability due to virtual inductors, virtual capacitors, and anti-windup," *IEEE Trans. Ind. Electron.*, vol. 64, no. 7, pp. 5994–6004, Jul. 2017.

[11] M. Ramezani, S. Li, F. Musavi, and S. Golestan, "Seamless transition of synchronous inverters using synchronizing virtual torque and flux linkage," *IEEE Trans. Ind. Electron.*, 2019, doi: 10.1109/TIE.2019.2892697.

[12] J. Roldan-Pérez, M. Prodanovic, and A. Rodríguez-Cabero, "Detailed discrete-time implementation of a battery-supported synchronverter for weak grids," in *Proc. 43rd Annu. Conf. IEEE Ind. Electron. Soc.*, Nov. 2017, pp. 1083–1088.

[13] S. Wang, J. Hu, X. Yuan, and L. Sun, "On inertial dynamics of virtual-synchronous-controlled DFIG-based wind turbines," *IEEE Trans. Energy Convers.*, vol. 30, no. 4, pp. 1691–1702, Dec. 2015.

[14] S. Dong and Y. C. Chen, "A method to directly compute synchronverter parameters for desired dynamic response," *IEEE Trans. Energy Convers.*, vol. 33, no. 2, pp. 814–825, Jun. 2018.

[15] H. Wu *et al.*, "Small-signal modeling and parameters design for virtual synchronous generators," *IEEE Trans. Ind. Electron.*, vol. 63, no. 7, pp. 4292–4303, Jul. 2016.

[16] W. Zhang, A. M. Cantarellas, J. Rocabert, A. Luna, and P. Rodriguez, "Synchronous power controller with flexible droop characteristics for renewable power generation systems," *IEEE Trans. Sustain. Energy*, vol. 7, no. 4, pp. 1572–1582, Oct. 2016.

[17] T. Shintai, Y. Miura, and T. Ise, "Oscillation damping of a distributed generator using a virtual synchronous generator," *IEEE Trans. Power Del.*, vol. 29, no. 2, pp. 668–676, Apr. 2014.

[18] L. Huang, H. Xin, H. Yang, Z. Wang, and H. Xie, "Interconnecting very weak ac systems by multiterminal VSC-HVDC links with a unified virtual synchronous control," *IEEE J. Emerg. Sel. Top. Power Electron.*, vol. 6, no. 3, pp. 1041–1053, Sep. 2018.

[19] Z. Shuai, Y. Hu, Y. Peng, C. Tu, and Z. J. Shen, "Dynamic stability analysis of synchronverter-dominated microgrid based on bifurcation theory," *IEEE Trans. Ind. Electron.*, vol. 64, no. 9, pp. 7467–7477, Sep. 2017.

[20] J. Liu, Y. Miura, H. Bevrani, and T. Ise, "Enhanced virtual synchronous generator control for parallel inverters in microgrids," *IEEE Trans. Smart Grid*, vol. 8, no. 5, pp. 2268–2277, Sep. 2017.

[21] D. Li, Q. Zhu, S. Lin, and X. Y. Bian, "A self-adaptive inertia and damping combination control of VSG to support frequency stability," *IEEE Trans. Energy Convers.*, vol. 32, no. 1, pp. 397–398, Mar. 2017.

[22] S. D'Arco, J. A. Suul, and O. B. Fosso, "Small-signal modeling and parametric sensitivity of a virtual synchronous machine in islanded operation," *Int. J. Elect. Power Energy Syst.*, vol. 72, pp. 3–15, 2015.

[23] S. D'Arco, J. A. Suul, and O. B. Fosso, "A virtual synchronous machine implementation for distributed control of power converters in smartgrids," *Electric Power Syst. Res.*, vol. 122, pp. 180–197, 2015.

[24] S. Dong and Y. C. Chen, "Adjusting synchronverter dynamic response speed via damping correction loop," *IEEE Trans. Energy Convers.*, vol. 32, no. 2, pp. 608–619, Jun. 2017.

[25] P. Kundur, N. Balu, and M. Lauby, *Power System Stability and Control* (ser. EPRI Power System Engineering Series). New York, NY, USA: McGraw-Hill, 1994.

[26] Q. C. Zhong and G. Weiss, "Synchronverters: Inverters that mimic synchronous generators," *IEEE Trans. Ind. Electron.*, vol. 58, no. 4, pp. 1259–1267, Apr. 2011.

[27] J. Roldan-Perez, A. Rodriguez-Cabero, and M. Prodanovic, "Harmonic virtual impedance design for parallel-connected grid-tied synchronverters," *IEEE J. Emerg. Sel. Top. Power Electron.*, vol. 7, no. 1, pp. 493–503, Mar. 2019.

[28] H. Akagi, E. H. Watanabe, and M. Aredes, *Instantaneous Power Theory and Applications to Power Conditioning*. Piscataway, NJ, USA: Wiley, 2007.

[29] J. M. Guerrero, J. Matas, L. Garcia De Vicunagarcia De Vicuna, M. Castilla, and J. Miret, "Wireless-control strategy for parallel operation of distributed-generation inverters," *IEEE Trans. Ind. Electron.*, vol. 53, no. 5, pp. 1461–1470, Oct. 2006.

[30] R. Pena-Alzola, M. Liserre, F. Blaabjerg, M. Ordonez, and T. Kerekes, "A self-commissioning notch filter for active damping in a three-phase LCL-filter-based grid-tie converter," *IEEE Trans. Power Electron.*, vol. 29, no. 12, pp. 6754–6761, Dec. 2014.

[31] A. Yazdani and R. Iravani, *Voltage-Sourced Converters in Power Systems*. Wiley, 2010.

[32] L. Zhang, L. Harnefors, and H. P. Nee, "Power-synchronization control of grid-connected voltage-source converters," *IEEE Trans. Power Syst.*, vol. 25, no. 2, pp. 809–820, May 2010.

[33] B. Kuo, *Automatic Control System*. London, U.K.: Prentice-Hall International, 1962.

[34] P. C. Krause, O. Wasynczuk, and S. D. Sudhoff, *Analysis of Electric Machinery and Drive Systems*, 2nd ed. Piscataway, NJ, USA: Wiley-IEEE Press, Feb. 2002.

[35] M. Abramowitz, *Handbook of Mathematical Functions, With Formulas, Graphs, and Mathematical Tables*. New York, NY, USA: Dover Publications, Incorporated, 1974.

[36] B. C. Kuo and F. Golnaraghi, *Automatic Control Systems*, 8th ed. New York, NY, USA: John Wiley & Sons Inc., 2002.

[37] K. J. Astrom and T. Hagglund, *PID Controllers: Theory, Design, and Tuning*, 2nd ed. Research Triangle Park, NC, USA: Int. Society for Measurement and Con, Jan. 1995.

[38] J. Wang, Y. Wang, Y. Gu, W. Li, and X. He, "Synchronous frequency resonance of virtual synchronous generators and damping control," in *Proc. 9th Int. Conf. Power Electron. ECCE Asia*, Jun. 2015, pp. 1011–1016.

[39] D. Yang, H. Wu, X. Wang, and F. Blaabjerg, "Suppression of synchronous resonance for VSGs," *J. Eng.*, vol. 2017, no. 13, pp. 2574–2579, 2017.

[40] F. Huerta, J. K. Gruber, M. Prodanovic, and P. Matatagui, "Power-hardware-in-the-loop test beds: Evaluation tools for grid integration of distributed energy resources," *IEEE Ind. Appl. Mag.*, vol. 22, no. 2, pp. 18–26, Mar. 2016.

Javier Roldán-Pérez (S'12–M'14) received the B.S. degree in industrial engineering, the M.S. degree in electronics and control systems, the M.S. degree in system modeling, and the Ph.D. degree in power electronics, all from Comillas Pontifical University, Madrid, Spain, in 2009, 2010, 2011, and 2015, respectively.

From 2010 to 2015, he was with the Institute for Research in Technology (IIT), Comillas University. In 2014, he was a Visiting Ph.D. Student at the Department of Energy Technology, Aalborg University, Denmark. From 2015 to 2016, he was with the Electric and Control Systems Department, Norvento Energía Distribuida, Spain. In September 2016, he joined the Electrical Systems Unit at IMDEA Energy Institute. His research interests include the integration of renewable energies, microgrids, and power electronics applications.

Alberto Rodríguez-Cabero received the degrees in industrial technical engineering and industrial engineering (specialized in electronics), and the master's degree in research in engineering systems modeling from the Comillas Pontifical University, Madrid, Spain, in 2011, 2013 and 2016, respectively.

From 2014 to 2015, he worked as at Control Engineer, Institute for Research in Technology (IIT), Comillas Pontifical University. Since September 2015, he has been working with the Electrical Systems Unit, Institute IMDEA Energy, Madrid, Spain. His research interests include the design and control of power electronics converters, power quality, and microgrids.

Milan Prodanovic (M'01) received the B.Sc. degree in electrical engineering from the University of Belgrade, Serbia, in 1996, and the Ph.D. degree from the Imperial College, London, U.K., in 2004.

From 1997 to 1999, he was with GVS Engineering Company, Serbia, developing UPS systems. From 1999 to 2010, he was a Research Associate with Electrical and Electronic Engineering Department, Imperial College, London, U.K. Currently, he is a Senior Researcher and Head of the Electrical Systems Unit, Institute IMDEA Energy, Madrid, Spain. His research interests include design and control of power electronics interfaces for distributed generation, microgrids control, and active management of distribution networks.